SEMAC: Slice Encoding for Metal Artifact Correction in MRI

Wenmiao Lu,[1,2]* Kim Butts Pauly,[1] Garry E. Gold,[1] John M. Pauly,[2] and Brian A. Hargreaves[1]

Magnetic resonance imaging (MRI) near metallic implants remains an unmet need because of severe artifacts, which mainly stem from large metal-induced field inhomogeneities. This work addresses MRI near metallic implants with an innovative imaging technique called "Slice Encoding for Metal Artifact Correction" (SEMAC). The SEMAC technique corrects metal artifacts via robust encoding of each excited slice against metal-induced field inhomogeneities. The robust slice encoding is achieved by extending a view-angle-tilting (VAT) spin-echo sequence with additional *z*-phase encoding. Although the VAT compensation gradient suppresses most in-plane distortions, the *z*-phase encoding fully resolves distorted excitation profiles that cause through-plane distortions. By positioning all spins in a region-of-interest to their actual spatial locations, the through-plane distortions can be corrected by summing up the resolved spins in each voxel. The SEMAC technique does not require additional hardware and can be deployed to the large installed base of whole-body MRI systems. The efficacy of the SEMAC technique in eliminating metal-induced distortions with feasible scan times is validated in phantom and in vivo spine and knee studies. Magn Reson Med 62:66–76, 2009.

Key words: distortion correction; metallic implants; metal artifacts; metal-induced distortions; susceptibility artifact; field inhomogeneities; distorted excitation profiles; view-angle-tilting.

Metallic implants, such as pedicle screws, are commonly used in orthopedic surgery to fixate fractures, replace arthritic joints, and to align and immobilize vertebra. In the United States alone, there were 325,000 spinal fusions performed in 2003 and 450,000 primary or revision total knee arthroplasties performed in 2002 (1). The current standard imaging test for complications associated with metallic implants is plain radiography. For accurate diagnosis, radiography requires the X-ray beam to be oriented exactly parallel to the bone-implant interface: any obliquity of the X-ray beam can obscure the radiolucent area (2). A better substitute for two-dimensional radiograph is cross-sectional imaging that images the entire bone-implant interface in three dimensions. However, the physical characteristics of metallic implants cause difficulties with cross-sectional imaging techniques. Computed tomography (CT) and invasive CT myelography suffer from metal-induced streak/beam-hardening artifacts and data loss throughout the field-of-view (FOV) (3). In addition, radiography and CT are relatively insensitive to soft tissue abnormalities and bone marrow edema caused by infection, which are important complications to be evaluated in patients with implants.

Magnetic resonance imaging (MRI) is potentially the best imaging modality for diagnosing patients with metallic implants because of its superior soft tissue contrast (4). However, MRI near metallic implants is hampered by severe artifacts, which stem from large metal-induced field inhomogeneities (5), local gradient-induced eddy currents on metal surfaces (6), and radiofrequency (RF) shielding effects (7). Among these, metal-induced field inhomogeneities are responsible for the most severe artifacts. It is well understood that steep field gradients near metal objects result in increased intra-voxel dephasing and a severely shortened T_2^*. As a result, MRI near metallic implants inevitably involves spin-echo (SE) sequences, which refocus the dephased spins. However, SE techniques still suffer from spatially dependent artifacts (e.g., signal voids and pile-ups), owing to a nonlinear frequency-position mapping caused by metal-induced field inhomogeneities. In the absence of field inhomogeneities, the mapping between a spin's precession frequency and its spatial location is a linear function (dotted line in Fig. 1), and the slope of the linear mapping is determined by the gradient amplitude. When metal-induced field inhomogeneities (dashed line of a bell shape in Fig. 1) superimpose upon the frequency induced by the gradient, the resulting frequency-position mapping becomes highly nonlinear (solid line in Fig. 1), which causes problems in slice-selective excitation and frequency encoding during the readout.

As illustrated in Fig. 1, an RF pulse with 1 kHz bandwidth centered at 11.5 kHz is designed to excite a 3-mm-thick slice centered at location 3.3 cm. However, because of the nonlinear frequency-position mapping, the RF pulse excites a much thinner slice centered at location 1.8 cm, resulting in through-plane displacement and signal loss due to the thinner slice. In a more extreme case, an RF pulse with 1 kHz bandwidth centered at 14.5 kHz excites spins centered around three locations (light gray regions

A preliminary account of this work was presented at the 16th Meeting of the International Society for Magnetic Resonance in Medicine, May, 2008, page 838.

[1]Department of Radiology, Stanford University, Stanford, California
[2]Department of Electrical Engineering, Stanford University, Stanford, California

Grant sponsor: NIH; Grant numbers: RR009784-11, EB002524-01, HL075803-01, CA077677-09, 2P41RR009784-11
Grant sponsor: Lucas Foundation

*Correspondence to: Wenmiao Lu, Department of Radiology, Lucas Center MC5488, Stanford, CA 94305-5488. E-mail: wenmiao.lu@gmail.com

Received 3 August 2008; revised 11 November 2008; accepted 4 January 2009.
DOI 10.1002/mrm.21967
Published online 6 March 2009 in Wiley InterScience (www.interscience.wiley.com).

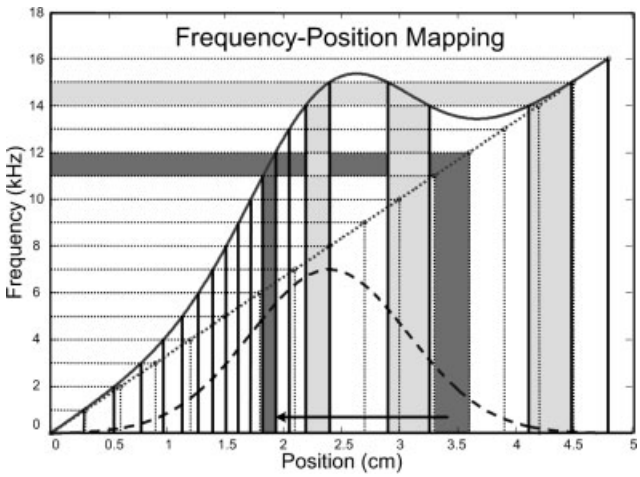

FIG. 1. In the absence of field inhomogeneities, the mapping between a spin's precession frequency and its spatial location is a linear function (dotted line), and the slope of the linear mapping is determined by the gradient amplitude. When metal-induced field inhomogeneities (dashed line of a bell shape) superimpose upon the gradient-induced frequency, the resulting frequency-position mapping becomes highly nonlinear (solid line), which causes problems in slice-selective excitation and frequency encoding during the readout. For example, an RF pulse with 1 kHz bandwidth centered at 11.5 kHz is designed to excite a 3-mm-thick slice centered at location 3.3 cm. However, under the nonlinear frequency-position mapping, this RF pulse excites a much thinner slice centered at location 1.8 cm, resulting in through-plane displacement and signal loss due to the thinner slice. In a more extreme case, a frequency band between 14 and 15 kHz maps to spins centered around three locations (light gray regions around 2.3, 3.1, and 4.4 cm), resulting in pile-ups.

around 2.3, 3.1, and 4.4 cm), resulting in through-plane pile-ups. This nonlinear frequency-position mapping can also be used to demonstrate the formation of in-plane distortions, when the gradient acts as a readout gradient. For example, the spins from the three light gray regions (around 2.3, 3.1, and 4.4 cm) are subject to the same frequency encoding, which leads to in-plane pile-ups along the readout direction. Based on the directions along which spatially dependent artifacts exist, the artifacts are grouped into through-plane distortions and in-plane distortions. These two types of distortions occur at different stages in a pulse sequence: through-plane distortions result from a distorted excitation profile during the slice-selective excitation, whereas in-plane distortions are due to disrupted frequency encoding during the readout.

Correction of metal-induced artifacts through postprocessing often relies on some assumptions about metal objects and field maps to unwrap the distortions. As it is difficult to have reliable estimation of field inhomogeneities around metal, these works only show success in obtaining in vivo MR images near tiny metallic objects (8) and may encounter difficulty in resolving pile-ups (9). In light of the distortions scaled with field strength, a prepolarized MRI (PMRI) system, which allows for low-field signal acquisition with mid-field signal-to-noise ratio (SNR), has been developed to image near metallic implants (10). However, the techniques developed for PMRI cannot be generalized to conventional whole-body systems (e.g., 1.5 T scanners). Currently, the most successful works on MRI near metallic implants are based on the view-angle-tilting (VAT) technique developed by Cho et al. (11). The work by Butts et al. (12) provides solutions to reduce VAT-associated blurring. In another work by Kolind et al. (13), a VAT-SE sequence with high RF and readout bandwidths is referred to as the "metal artifact reduction sequence" (MARS), which produces promising MR images near metal objects. However, these advances in employing VAT for imaging near metal objects only address the correction of in-plane distortions. Except the work by Butts et al. (9) that resamples slice profiles based on field maps, the work by Koch et al. (14) that performs multiple frequency offset acquisitions, and our preliminary work (15), most methods suffer from through-plane distortions.

In this work, we address both in-plane and through-plane distortions with an innovative imaging technique called "Slice Encoding for Metal Artifact Correction" (SEMAC). The SEMAC technique corrects metal artifacts via robust encoding of each excited slice against metal-induced field inhomogeneities. The robust encoding is achieved by extending a VAT-SE sequence with additional phase encoding along the slice-select z-axis (15), as shown in Fig. 2. Although the VAT-compensation gradient suppresses most in-plane distortions, the additional z-phase encoding is included to fully resolve a complicated distorted excitation profile of each slice. By positioning all spins in a region-of-interest to their actual spatial locations, the through-plane distortions can be corrected by summing up the resolved spins in each voxel. To avoid SNR degradation of the results obtained from the SEMAC technique, the relative phases between slices must be eliminated such that the spins resolved from different slices can be coherently summed without taking the magnitude operation. The SEMAC technique does not require additional hardware and can be deployed to the large installed base of whole-body MRI systems. The efficacy of the SEMAC technique in eliminating metal-induced distortions with feasible scan times is validated in phantom and in vivo spine and knee studies.

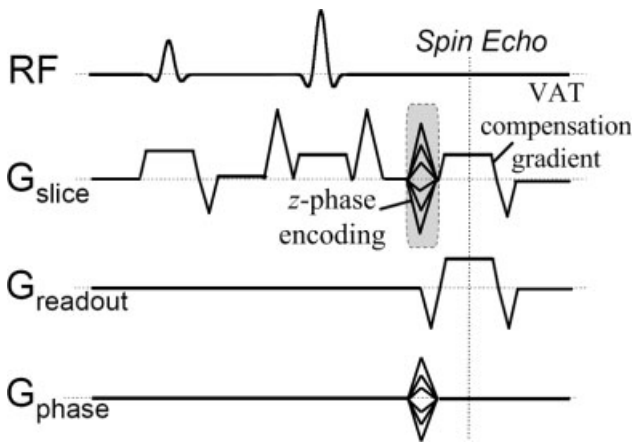

FIG. 2. Schematic diagram of the SEMAC sequence for imaging near metallic implants. The VAT compensation gradient suppresses in-plane distortions, whereas the additional z-phase encoding steps are included to resolve distorted excitation profiles that cause through-plane distortions.

METHODS AND MATERIALS

Let $m(x,y,z)$ and $\Delta f(x,y,z)$ denote spin density and field inhomogeneity at a voxel location (x,y,z), where x and z are assumed to be readout and slice-select directions, respectively. As there is no distortion along the phase-encoding y-axis, we drop the dependence of $m(x,y,z)$ and $\Delta f(x,y,z)$ on y for notational simplicity in the remainder of this section.

Distorted Excitation Profile

We first consider the effect of the field inhomogeneity $\Delta f(x,z)$ during slice-selective excitation. Given an RF pulse of bandwidth B_{RF} and a slice-select gradient of amplitude G_{s}, the excited magnetization m_e is given by:

$$\begin{aligned} m_{\mathrm{e}}(x,z) &= m(x,z)\cdot\sqcap\left[\frac{\frac{\gamma}{2\pi}G_{\mathrm{s}}z+\Delta f(x,z)-f_{\mathrm{e}}}{B_{\mathrm{RF}}}\right] \\ &= m(x,z)\cdot\sqcap\left[\frac{z-\Delta z(x,z)-z_0}{s}\right], \end{aligned} \quad [1]$$

where z_0 is the nominal slice location excited at a transmit frequency $f_{\mathrm{e}}=\frac{\gamma}{2\pi}G_{\mathrm{s}}z_0$, and $\frac{\gamma}{2\pi}$ is the gyromagnetic ratio equal to 42.58 MHz/Tesla for ^{1}H. The through-plane shift Δz for a spin with field inhomogeneity Δf is

$$\Delta z = -\frac{\Delta f}{\frac{\gamma}{2\pi}G_{\mathrm{s}}} = -\frac{\Delta f}{B_{\mathrm{RF}}}s, \quad [2]$$

where $s=2\pi B_{\mathrm{RF}}/(\gamma G_{\mathrm{s}})$ is the nominal slice thickness. $\sqcap(f/B_{\mathrm{RF}})$ is the frequency profile of the RF pulse, which ideally is a rectangular function defined by

$$\sqcap(f/B_{\mathrm{RF}}) = \begin{cases} 1, & \text{if } |f| \le B_{\mathrm{RF}}/2 \\ 0, & \text{otherwise.} \end{cases}$$

The metal-induced field inhomogeneities cause the excited magnetization $m_{\mathrm{e}}(x,z)$ to contain spins from different slice locations, for which $|z-\Delta z(x,z)-z_0| \le s/2$. Therefore, $\Delta z(x,z)$ represents the distorted excitation profile caused by the field inhomogeneity $\Delta f(x,z)$.

Figure 3 illustrates that distorted excitation profiles can lead to severe through-plane distortions. Figure 3a depicts a simulated dipole pattern of metal-induced field inhomogeneities (16), where the sample field inhomogeneities along the x-axis (solid line) and along the z-axis (dashed line) are plotted in Fig. 3b. When the field inhomogeneities superimpose upon the frequency induced by the slice-select gradient, the resulting excitation profiles correspond to the frequency bands shown in Fig. 3c. The spins are excited when their precession frequencies fall into the corresponding frequency bands, and the excitation profiles of three sample slices are shown in Fig. 3d–f. As the excited slices contain spins from different slice locations, the distorted excitation profiles lead to through-plane distortions.

SEMAC Sequence

Figure 2 shows the proposed pulse sequence, in which the z-phase encoding steps are included to resolve the distorted excitation profile of each slice. Given N_z z-phase encoding steps with an incremental amplitude of G_{zi} and a duration of T_z, the resolution of z-phase encoding is $\delta_{\mathrm{s}}=2\pi/(\gamma N_z G_{zi} T_z)$. Besides the z-phase encoding, we also apply a VAT-compensation gradient of the amplitude G_{s} during the readout (11). At the readout time t and the n^{th} z-phase encoding step, the received signal $r(t,n)$ is given by:

$$\begin{aligned} r(t,n) = &\int_z\left(\int_x m_{\mathrm{e}}(x,z)exp[-i(\gamma G_x x+\gamma G_{\mathrm{s}}z+2\pi\Delta f(x,z))t]dx\right) \\ &\times exp[-in\gamma G_{zi}T_z z]dz. \end{aligned}$$

Let us examine the effects of the VAT-compensation gradient during the readout:

$$\begin{aligned} &\int_x m_{\mathrm{e}}(x,z)exp[-i(\gamma G_x x+\gamma G_{\mathrm{s}}z+2\pi\Delta f(x,z))t]dx \\ &=\int_x m_{\mathrm{e}}(x,z)exp[-i(\gamma G_x x+\gamma G_{\mathrm{s}}(z-\Delta z(x,z)-z_0)+2\pi f_{\mathrm{e}})t]dx \\ &=\int_x m_{\mathrm{e}}(x,z_l)exp\left[-i\left(\gamma G_x\left(x+\frac{G_{\mathrm{s}}}{G_x}\delta z(x,z)\right)+2\pi f_{\mathrm{e}}\right)t\right]dx, \end{aligned} \quad [3]$$

where $\delta z(x,z)=z-z_0-\Delta z(x,z)$ is the ambiguity in determining the slice locations of the spins in the distorted slice and $|\delta z| \le s/2$ (see Eq. [1]). Equation [3] shows that δz is responsible for uncorrected in-plane spin distortions $\delta x=\frac{G_{\mathrm{s}}}{G_x}\delta z$, as the encoded x-location is given by

$$x' = x+\frac{G_{\mathrm{s}}}{G_x}\delta z(x,z) = x+\delta x(x,z). \quad [4]$$

When expressed in terms of pixels, the uncorrected in-plane spin distortion is bounded by

$$\delta x_{\max} = \frac{B_{\mathrm{RF}}/2}{B_{\mathrm{p}}}, \quad [5]$$

where $B_{\mathrm{p}}=2B_{\mathrm{read}}/N_x$ is the readout bandwidth per pixel. (B_{read} and N_x are the readout bandwidth and the number of readout samples, respectively.) In a typical imaging case, 1 kHz RF bandwidth, ±125 kHz readout bandwidth and 256 readout samples limit the maximum in-plane spin distortion to be less than 0.512 pixels with the VAT compensation gradient. Referring to the through-plane distortion Δz (Eq. [2]) and the maximum in-plane spin distortion δx with the VAT technique (Eq. [5]), it can be seen that the selection of the RF bandwidth B_{RF} forces a tradeoff between Δz and δx (cf. Discussion).

Equation [3] shows that the VAT-compensation gradient also modulates the excited spins at the transmit frequency f_{e} during the readout. In the case of exciting multiple slices, we need to demodulate each slice with its transmit frequency accordingly such that the slices do not have relative in-plane shifts. The received signal $r(t,n)$ demodulated at f_{e} is given by

$$\begin{aligned} r(t,n) &= \int_z\left(\int_x m_{\mathrm{e}}(x,z)exp[-i\gamma G_x(x+\delta x(x,z))]dx\right) \\ &\quad\times exp[-ink_{zi}z]dz \\ &= \int_z\left(\int_x m_{\mathrm{e}}(x,z)exp[-i\gamma G_x x't]dx\right)exp[-ink_{zi}z]dz, \end{aligned} \quad [6]$$

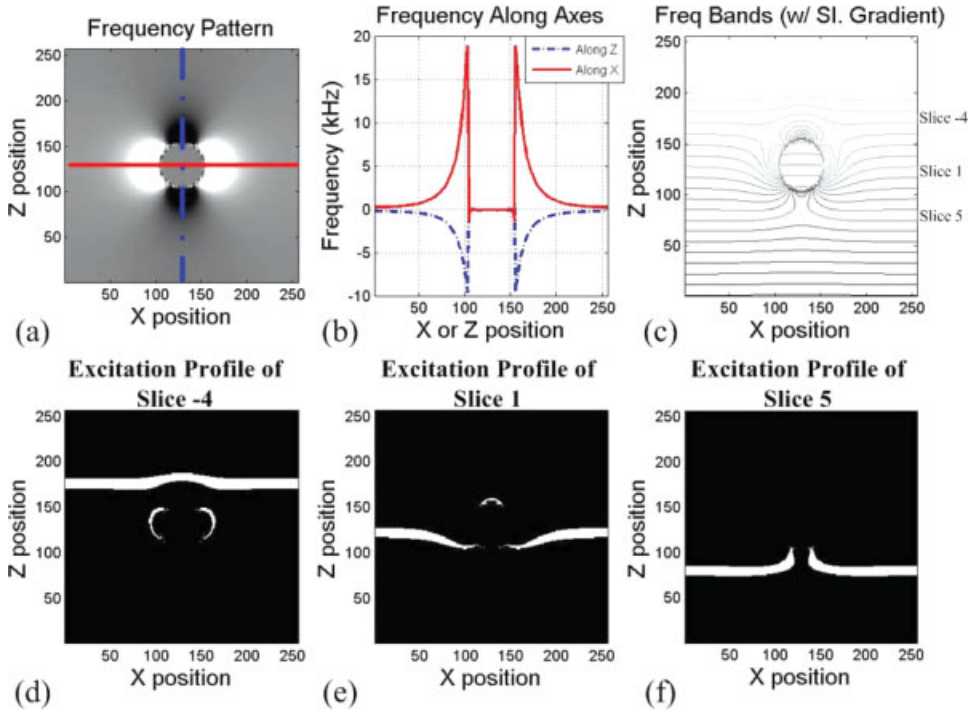

FIG. 3. Illustration of severe through-plane distortions caused by distorted excitation profiles. (**a**) Simulated dipole pattern of metal-induced field inhomogeneities from a cylindrical object, where the sample field inhomogeneities along the *x*-axis (solid line) and along the *z*-axis (dashed line) are plotted in (**b**). When the field inhomogeneities superimpose upon the frequency induced by the slice-select gradient, the resulting excitation profiles correspond to the frequency bands shown in (**c**). The bottom three sample distorted excitation profiles in (**d**–**f**) show that the spins are excited when their precession frequencies fall into the frequency bands (highlighted in gray in (c)) corresponding to the excited slices. As the excited slices contain spins from different slice locations, the distorted excitation profiles lead to through-plane distortions. [Color figure can be viewed in the online issue, which is available at www.interscience.wiley.com.]

where $k_{zi} = \gamma G_{zi} T_z$ is the *z*-phase encoding increment. The *z*-phase encoding FOV_z is given by $2\pi/k_{zi}$, which should be sufficiently large to avoid aliasing in the resolved excitation profile.

Correction of Through-plane Distortions

Equation [6] shows that the proposed SEMAC sequence enables robust spatial encoding against metal-induced field inhomogeneities. An inverse Fourier transform of the received signal $r(t, n)$ completely resolves the spatial distribution of the magnetization $m_e(x, z)$. When distorted excitation profiles result in through-plane distortions, pile-ups in one slice correspond to signal voids in other slices. Hence, multiple slices are required in the correction of through-plane distortions. Figure 4 illustrates the working principle of the SEMAC technique. During the image acquisition, the metal-induced field inhomogeneities result in complicated distorted excitation profiles (highlighted in different colors). The number of the slices, N_S, is chosen to cover all spins inside a region-of-interest (ROI). For each slice, its excitation profile is resolved with the *z*-phase encoding. During the image reconstruction, the spins in the ROI are positioned back to their actual voxel locations. Subsequently, the through-plane distortions can be corrected by summing up the spins in each voxel.

In practice, direct summation usually results in severe signal loss, as the spins resolved from different slices can have relative phases. The relative phases between slices can be understood by examining Eq. [3], where the VAT-compensation gradient modulates the spin echo in each slice to the corresponding RF transmit frequency. As the spins excited in different slices precess at different RF transmit frequencies, any timing mismatch in echo acquisition results in relative phases between the slices. While summing the magnitudes of the resolved spins removes the relative phases between slices, the magnitude operation causes the background noise to become Rayleigh-distributed, which is no longer zero-mean (17). Summing the nonzero mean noise degrades the resultant signal-to-noise ratio (SNR). In this work, we eliminate the timing mismatch in echo acquisition by carefully adjusting the RF phase reference and/or the receive phase reference (18). When no relative phase exists between the slices, the resolved spins in each voxel can be coherently summed without taking the magnitude operation.

SNR Analysis

To evaluate the SNR performance of the SEMAC technique, we consider an impulse object located at the origin (i.e., $x = 0$ and $z = 0$). To simplify the analysis, we assume that no field inhomogeneity disrupts slice-selective excitation and frequency encoding; hence, all SNR evaluations are conducted at the pixel that corresponds to the voxel centered at the origin. A one-dimensioned reconstruction

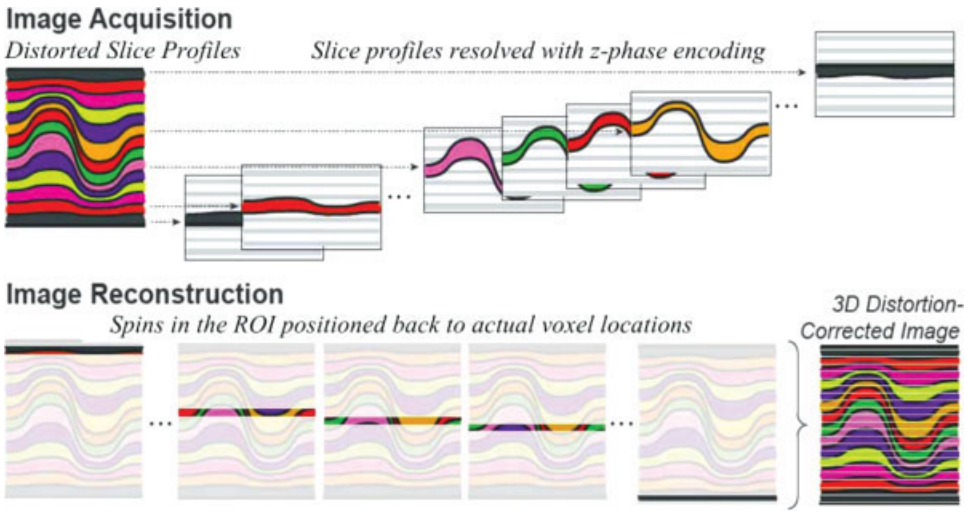

FIG. 4. Illustration of the correction of through-plane distortions in the SEMAC technique. During the image acquisition, the metal-induced field inhomogeneities result in complicated distorted slice excitation profiles (highlighted in different colors). For each slice, its excitation profile is resolved with the z-phase encoding over the FOV shown. During the image reconstruction, the signals resolved from different excited slices are combined at each voxel location such that the through-plane distortions are completely corrected.

of the object is taken as the reference case for SNR evaluation. The impulse object gives rise to a constant signal amplitude M for each of the N_x readout samples. Without taking the magnitude operation, each readout sample contains zero-mean white Gaussian noise with variance σ_n^2. The SNR of the 1D reconstruction is given by

$$\mathrm{SNR}_{\mathrm{SE}} = \frac{\sum_{j=1}^{N_x} M}{\sqrt{\sum_{j=1}^{N_x} \sigma_n^2}} = \frac{\sqrt{N_x} M}{\sigma_n},$$

which is the SNR of the reconstructed impulse object obtained from a standard spin-echo sequence or a VAT-SE sequence.

The SEMAC sequence imposes the readout samples obtained from a VAT-SE sequence with z-dependent phase factors. As the impulse object resides at the origin, the slice location is $z = 0$; hence, all z-dependent phase factors are equal to 1. Therefore, for imaging this impulse object, the SEMAC sequence essentially repeats the VAT-SE sequence for N_z times. (N_z is the number of z-phase encoding steps.) The reconstruction of the impulse object is achieved with an inverse 2D Fourier transform evaluating at the origin, and the SNR with the SEMAC sequence is given by

$$\mathrm{SNR}_{\mathrm{SEMAC}} = \frac{\sum_{i=1}^{N_z} \sum_{j=1}^{N_x} M}{\sqrt{\sum_{i=1}^{N_z} \sum_{j=1}^{N_x} \sigma_n^2}} = \frac{\sqrt{N_z N_x} M}{\sigma_n},$$

which shows that the SNR is improved by $\sqrt{N_z}$, given the longer scan time.

The gain in SNR with the SEMAC sequence is, however, reduced by the correction of through-plane distortions that involves summing multiple slices. Each slice has a z-phase encoding FOV ($\mathrm{FOV}_z = N_z \delta_s$), which is centered at its nominal slice location. The relative shift along the slice-select z-axis is the nominal slice thickness between two neighboring slices. In our implementation, the z-phase encoding resolution is set to be the same as the nominal slice thickness; hence, the voxel corresponding to the origin can be covered by as many as N_z slices. Although the impulse object only gives rise to nonzero signal amplitude for the slice that is centered at the origin, all k-space samples contain independent noise with variance σ_n^2. Consequently, the correction of through-plane distortion, which sums the resolved signal from different slices, results in an increase in noise variance. The resultant SNR is given by

$$\widetilde{\mathrm{SNR}}_{\mathrm{SEMAC}} = \frac{\sum_{i=1}^{N_z} \sum_{j=1}^{N_x} M}{\sqrt{\sum_{k=1}^{N_z} \sum_{i=1}^{N_z} \sum_{j=1}^{N_x} \sigma_n^2}} = \frac{\sqrt{N_x} M}{\sigma_n},$$

which is the same as the reference SNR obtained from the SE or VAT-SE sequence.

The above analysis shows that the SNR performance of the SEMAC technique is adversely affected by the number of slices involved in the correction of through-plane distortions. Therefore, the correction of through-plane distortions at a voxel should only involve the slices that contain the signals arising from this voxel. To that end, a heuristic threshold is selected to differentiate the signals from background noise. As the signals are generally much stronger than background noise and the frequency dispersion in each voxel is limited, the threshold is the median magnitude of all spins resolved from multiple slices. Only the spins with magnitudes greater than the threshold are included in the correction of through-plane distortions. In our experience, this threshold achieves a good balance between the correction of through-plane distortions and the exclusion of background noise.

EXPERIMENTAL METHODS

All experiments were performed on a GE Signa 1.5 T scanner (General Electric Healthcare, Waukesha, WI) with gradients capable of 40 mT/m amplitude and 150 T/m/sec

slew rate, and a readout bandwidth up to ±250 kHz. Reconstruction and postprocessing were performed off-line in MATLAB (Mathworks, South Natick, MA). Windowed-SINC pulses with pulse duration 3.2 ms were used as both the 90° excitation pulse and the 180° refocusing pulse in the SEMAC sequence. The amplitude of the 180° refocusing pulse is twice that of the 90° excitation pulse. To alleviate the VAT-associated blurring, the readout bandwidths were chosen such that the readout duration matched the main lobe of the RF pulses (12); however, the relatively high readout bandwidths (i.e., greater than 100 kHz) lower the SNR of the resultant images. The number of slices and the nominal slice thickness were chosen to cover all spins in the region-of-interest. Multiple slices were excited and acquired in an interleaved manner. In the following experiments, 16 *z*-phase encoding steps were prescribed for each slice to resolve the slice excitation profile. For evaluation purposes, each of the following experiments was repeated with a spin-echo (SE) sequence and a VAT-SE sequence (by turning off the *z*-phase encoding steps), while keeping all other scan parameters the same as the SEMAC sequence.

Phantom Experiments

For phantom evaluation, the SEMAC technique was used to image a titanium shoulder prosthesis immersed in agar gel using a quadrature head coil and the following scan parameters: TE/TR = 11/400 msec, acquisition matrix = 256 × 128, FOV = 20 cm, readout bandwidth ±125 kHz, nominal slice thickness 2 mm with no gap between slices. The time-bandwidth product (TBW) of the RF pulse is 4, which gives the RF bandwidth $B_{RF} = 1.25$ kHz. There are 16 *z*-phase encoding steps per slice, which account for ±10 kHz (i.e., $\pm 8B_{RF}$) field inhomogeneities in each slice. To cover a volume containing the metallic implants, 22 slices were prescribed and 14 min scan time was incurred.

In Vivo Experiments

For in vivo experiments, the SEMAC technique was used to image two subjects with metallic implants in their spines and one subject with several stainless steel screws in his lower leg. For imaging of the first subject with scoliosis rods in her spine, an eight-channel phased-array Cervical-Thoracic-Lumbar (CTL) coil and the following scan parameters were used: TE/TR = 11/523 msec, acquisition matrix = 256×128, FOV = 28 cm, readout bandwidth ±166 kHz, nominal slice thickness 3 mm with no gap between slices. The TBW of the RF pulse is 6.4, which gives the RF bandwidth $B_{RF} = 2$ kHz. There are 16 *z*-phase encoding steps per slice, which account for up to ±16 kHz (i.e., $\pm 8B_{RF}$) field inhomogeneities in each slice. To cover the spine and the implants, 32 slices were prescribed, resulting in an 18 min scan time.

For imaging of the second subject with a metallic fixation device in his spine, an eight-channel phased-array CTL coil and the following scan parameters were used: TE/TR = 11/400 msec, acquisition matrix 256 × 128, FOV = 24 cm, readout bandwidth ±125 kHz, nominal slice thickness 4 mm with no gap between slices. The TBW of the RF pulse is 4, which gives the RF bandwidth $B_{RF} = 1.25$ kHz. There are 16 *z*-phase encoding steps per slice, which account for up to ±10 kHz field inhomogeneities in each slice. To cover the spine and the device, 22 slices were prescribed. This study took a 14 min scan time.

The last leg study used an eight-channel transmit/receive knee coil and the following scan parameters: TE/TR = 12/555 msec, acquisition matrix = 256 × 128, FOV = 32 cm, readout bandwidth ±166 kHz, nominal slice thickness 4 mm with no gap between slices. The TBW of the RF pulse is 6.4, which gives the RF bandwidth $B_{RF} = 2$ kHz. There are 16 *z*-phase encoding steps per slice, which account for up to ±16 kHz field inhomogeneities in each slice. To cover a volume containing the knee, 32 slices were prescribed and 18 min scan time was incurred.

RESULTS

Figure 5 shows the phantom results obtained from the SE sequence, the VAT-SE sequence, and the SEMAC technique. When compared with the photo of the prosthesis, the SEMAC technique successfully recovers the shape of the prosthesis by suppressing severe distortions present in the results obtained from the SE sequence and the VAT-SE sequence. The first three rows show the comparison of the in-plane results. Despite partial correction of the distortions in the results obtained with the SE sequence, the VAT-SE sequence still suffered from uncorrected through-plane distortions, which occlude the features of the cobalt-chrome head of the prosthesis. In contrast, the SEMAC technique correctly reproduced the shape and fine details of the prosthesis. The improvement produced by the SEMAC technique can also be clearly visualized by comparing the reformatted results in the bottom row.

This phantom study was also used to evaluate the SNR performance of the SEMAC technique when compared with those of the SE and VAT-SE sequences. The SNR evaluation was conducted by selecting an uniform region in the in-plane results of a sample slice (identified with dashed boxes in Fig. 5). The SNR of each technique was empirically computed as the ratio of the average signal magnitude in the selected region to the standard deviation of background noise. The empirical SNRs of the SE sequence, the VAT sequence, and the SEMAC technique are 22, 22, and 34, respectively. Hence, by excluding background noise from the correction of through-plane distortions, we improve the SNR performance of the SEMAC technique.

Figure 6 shows the in vivo results of the subject with scoliosis rods in her spine. When compared with the SE (the first row) and VAT-SE (the second row) sequences, the SEMAC technique (the bottom row) achieved distortion-free imaging of the scoliosis rods. As noted by arrows in the first and third columns, the SEMAC technique managed to produce perfect delineation of the rods and pedicle hooks, which is important for determining if there is any displacement of the implants. In the second column, the SEMAC technique recovered the spinal cord, otherwise occluded in the results obtained from the SE and VAT-SE sequences, which is critical for evaluating spinal complications associated with the implants. The rightmost column in Fig. 6 shows the sample coronal reformats of the results, which demonstrate the efficacy of the SEMAC technique in

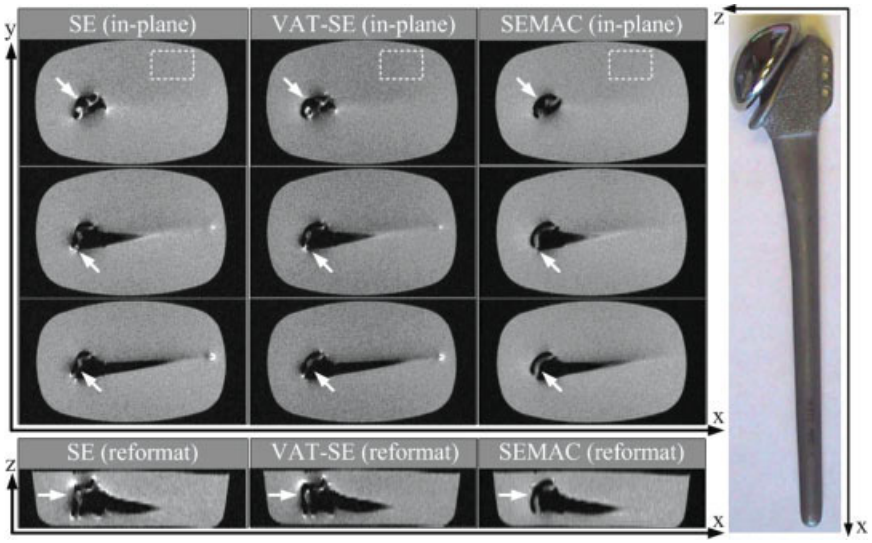

FIG. 5. Comparison of the phantom results obtained from the SE sequence, the VAT-SE sequence, and the SEMAC technique. The first three rows show the comparison of the in-plane results. The dashed boxes in the first row select an uniform region for SNR evaluation of the different techniques. Despite partial correction of the distortions in the results obtained with the SE sequence, the VAT-SE sequence still suffers from uncorrected through-plane distortions, which occlude the features of the cobalt-chrome head of the prosthesis (noted by arrows). In contrast, the SEMAC technique correctly reproduces the shape and fine details of the prosthesis. The improvement produced by the SEMAC technique can also be clearly visualized by comparing the reformatted results in the bottom row. With the elimination of almost all metal-induced distortions, the rounded shape of the implant head is recovered. [Color figure can be viewed in the online issue, which is available at www.interscience.wiley.com.]

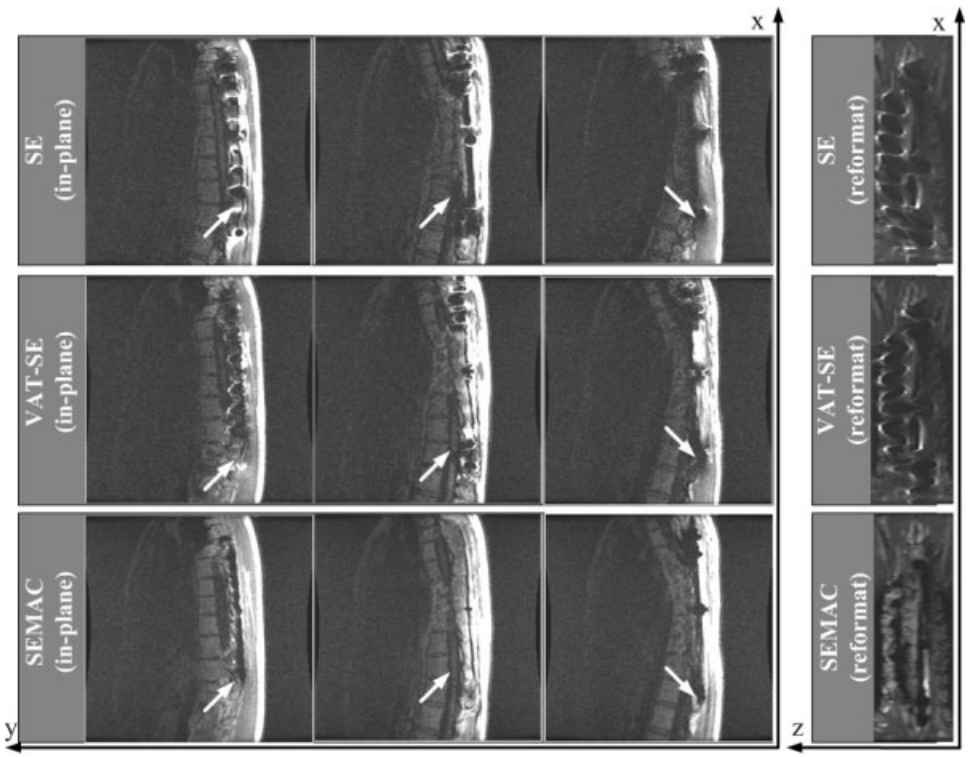

FIG. 6. Comparison of in vivo results of the subject with scoliosis rods in her spine. The results were obtained from the SE sequence, the VAT-SE sequence, and the SEMAC technique. In comparison with the SE (the first row) and VAT-SE (the second row) sequences, the SEMAC technique (the bottom row) achieves distortion-free imaging of the scoliosis rods. As pointed by arrows in the first and third columns, the SEMAC technique managed to produce perfect delineation of the rods and pedicle hooks. In the second column, the SEMAC technique recovers the spinal cord occluded in the results obtained from the SE and VAT-SE sequences. The rightmost column shows the sample coronal reformats of the results, which demonstrate the efficacy of the SEMAC technique in eliminating the severe metal-induced distortions.

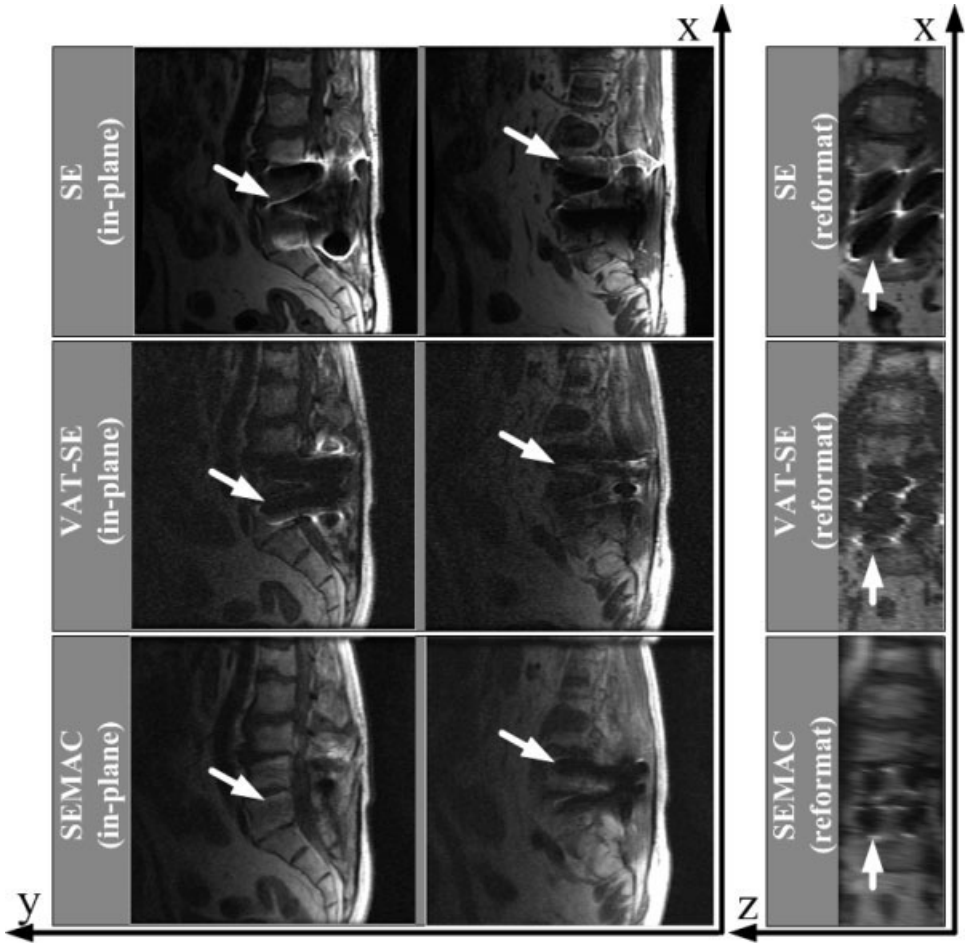

FIG. 7. Comparison of in vivo results of the subject with a metallic fixation device in his spine. When compared with the SE (the first row) and the VAT-SE (the second row) sequences, the SEMAC technique (the bottom row) greatly suppresses the metal-induced distortions. The in-plane sample results show that the SEMAC technique recovers the entire spine (leftmost column) and delineates the fixation device (middle column). As shown in the coronal reformats of the results (rightmost column), the SEMAC technique reveals the four poles of the devices that cannot be seen with the SE and VAT-SE sequences.

correcting the metal-induced distortions hampering the SE and VAT-SE sequences.

Figure 7 shows the in vivo results of the subject with a metallic fixation device in his spine. The results were obtained from the SE sequence (top row), the VAT-SE sequence (middle row), and the SEMAC technique (bottom row). The SEMAC technique recovers the entire spine in the leftmost column and delineates the fixation device in the middle column, which cannot be seen with the SE and VAT-SE sequences. The rightmost column shows the coronal reformats of the results; the SEMAC technique eliminates the severe distortions and reveals the four poles of the fixation device that are occluded by the metal-induced distortions with the SE and VAT-SE sequences. Note that small blurring exists in the coronal reformat of the SEMAC result, due to the prescription of the relative thick (4 mm) nominal slice thickness.

Figure 8 shows the in vivo results of the subject with several stainless steel screws in his lower leg. The results were obtained from the SE sequence (top row), the VAT-SE sequence (middle row), and the SEMAC technique (bottom row). With the SEMAC technique, the screws can be clearly visualized in both the in-plane results and the reformatted coronal view. In this study, the stainless steel screws result in such severe metal-induced field inhomogeneities that some resulting through-plane distortions fall outside the volume covered by the prescribed slices. The insufficient coverage of the spins leads to the signal loss, as evident by partial recovery of the rounded shapes of the drilled holes. In addition, the remaining uncorrected in-plane distortions manifest in the forms of ripple patterns (dotted arrows), which need to be addressed with stronger slice-select and/or readout gradients. Nevertheless, the SEMAC technique greatly suppresses the severe metal-induced distortions such that images with diagnostic value are obtained.

DISCUSSION

The main difficulty in MRI near metallic implants results from large metal-induced field inhomogeneities, which vary with implant materials, implant sizes/shapes, and implant orientations with respect to main magnetic field (19). As metal-induced field inhomogeneities cannot be

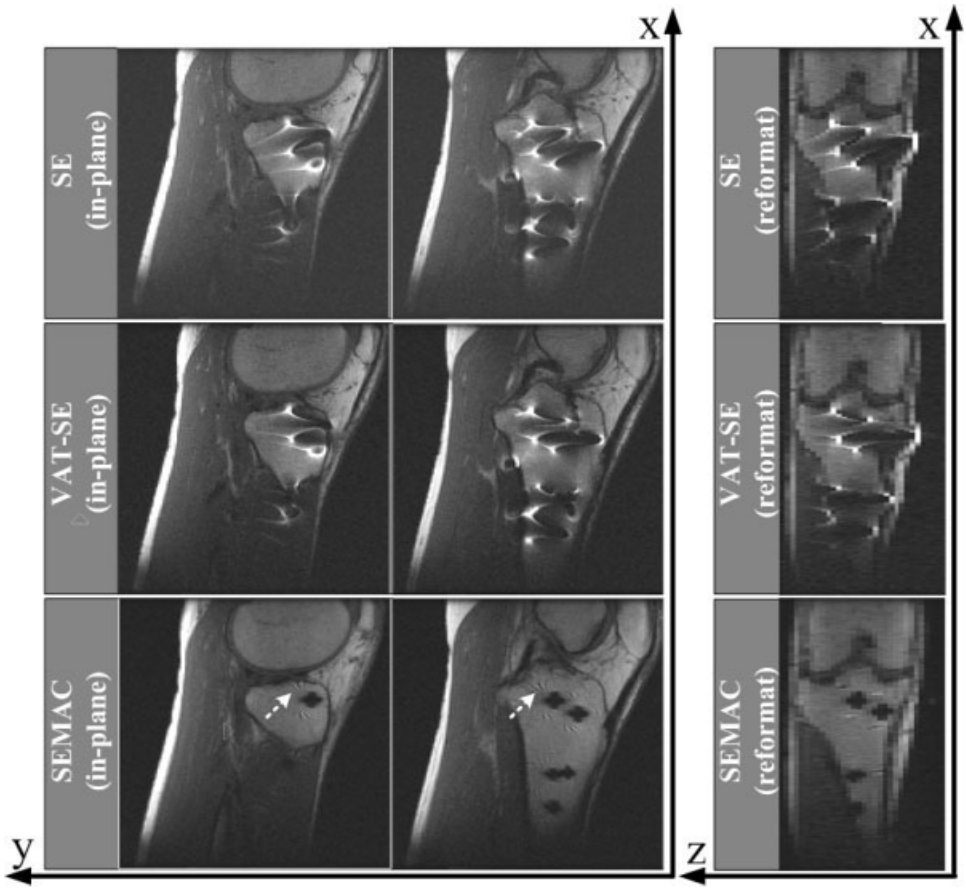

FIG. 8. Comparison of in vivo results of the subject with stainless steel screws in his lower leg. When compared with the SE (the first row) and the VAT-SE (the second row) sequences, the SEMAC technique (the bottom row) greatly suppresses the metal-induced distortions. As can be seen from the in-plane sample results and the reformatted coronal views, the SEMAC technique enables the clear visualization of the screws, which cannot be seen with the SE and VAT-SE sequences. Because of the sheer field inhomogeneities induced by the stainless steel, some spins fall outside the volume covered by the prescribed slices. This leads to partial recovery of the rounded shapes of the drilled holes. In addition, the remaining uncorrected in-plane distortions manifest in the forms of ripple patterns (dotted arrows), which need to be addressed with stronger slice-select and/or readout gradients.

accurately modeled in general, distortion-free MRI near metallic implants should rely on robust spatial encoding. A brute-force approach is to employ 3D phase encoding that incurs prohibitively long scan times (20). In this work, we propose an innovative imaging technique called SEMAC, which consists of a novel imaging sequence and a postprocessing procedure to correct through-plane distortions.

The proposed SEMAC sequence, which provides robust encoding against metal-induced field inhomogeneities with a feasible scan time, is derived from several existing susceptibility imaging techniques. Specifically, spin-echo (SE) addresses the signal losses due to intra-voxel dephasing and the VAT-compensation gradient suppresses in-plane distortions. The additional z-phase encoding is closely related to z-shim technique used in functional MRI (21,22) and gradient-echo slice excitation profile imaging (GESEPI) by Yang et al. (23). In comparison to the z-shim technique that mainly deals with a linear field variation along the slice-select direction, the SEMAC technique corrects arbitrary field variations induced by metal. Although GESEPI has been an effective means to recover the signal loss caused by intra-voxel dephasing in gradient-echo sequences, the SEMAC technique addresses large and arbitrary metal-induced field inhomogeneities that cause through-plane distortions across many slices.

Scan Parameters

The RF bandwidth in the SEMAC sequence is an important scan parameter that determines a tradeoff between suppressing in-plane distortions and resolving through-plane distortions. The VAT compensation gradient forces each excited spin to precess at the same Larmor frequency during the slice-selective excitation and the readout; hence, the metal-induced field inhomogeneities Δf are effectively compressed within the RF bandwidth B_{RF}. As $B_{RF} \ll \Delta f$ for imaging near metallic implants, the in-plane distortions are almost completely suppressed. From Eq. [5], increasing the readout bandwidth per pixel B_p and/or reducing the RF bandwidth B_{RF} can further improve the correction of in-plane distortions. However, a larger B_p leads to a loss in SNR, and a lower RF bandwidth leads to more severe through-plane distortions that require more slices to be acquired with a larger z-phase encoding FOV.

Through-plane distortions can only be fully corrected when all spins in a region-of-interest (ROI) are excited and spatially encoded. For an efficient coverage of the spins, we need to choose both nominal slice thickness s and the number of slices N_S such that sN_S is large enough to contain the largest through-plane distortion. The through-plane distortions are measured by reformatting the images obtained from the VAT-SE sequence in the (x, z) image plane. In general, for a given number of slices N_S, the full coverage of all spins in the ROI should be provided while prescribing the thinnest possible nominal slice thickness. This is because thin nominal slice thickness requires a strong slice-select gradient, which reduces the through-plane distortions.

There are two scan parameters related to resolving excitation profiles, namely, the number of z-phase encoding steps N_z and the z-phase encoding resolution δ_s. In the current implementation, the z-phase encoding resolution is set to the nominal slice thickness; i.e., $\delta_s = s$. In this case, the number of z-phase encoding steps N_z should give a sufficiently large z-phase encoding FOV, which covers the through-plane distortions across $\pm\Delta f_{max}/B_{RF}$ slices. Δf_{max} is the maximum metal-induced field inhomogeneity that can be measured with a spectroscopical prescan with all phase-encoding gradients and the readout gradient turned off. Although setting $\delta_s = s$ is sufficient for most cases, we expect that the correction of through-plane distortions can be further improved with a higher z-phase encoding resolution. However, a higher z-phase encoding resolution requires more z-phase encoding steps to maintain the same z-phase encoding FOV, which leads to longer scan times.

Although the reported experiments use T_1-weighted imaging performed on 1.5 T scanners, the SEMAC technique can be used to image near metallic implants at a high field strength (e.g., 3 T) and/or with T_2 contrast. Because more severe distortions exist at a high field strength, a longer scan time is incurred to acquire more slices with a larger z phase encoding FOV. As the SEMAC technique involves exciting multiple slices with no gap in between, the cross-talk between the slices reduces the effective TR, which in turn could affect T_2 or proton density weighted imaging. The shortened effective TR can be addressed by designing RF pulses with exceptionally sharp slice profiles or prescribing longer repetition intervals. In addition, the SEMAC technique is compatible with extended echo train sequences, such as fast spin echo with extended echo train acquisition (FSE XETA) (24), which will lead to a more flexible tradeoff between contrast and scan times.

Acceleration Techniques

For future work, to maintain feasible scan times or to achieve better correction of distortions, the SEMAC sequence will be incorporated with fast imaging techniques, such as partial k-space acquisition (25) along the phase-encoding y-axis. Exploiting the fact that the order of a multidimensional Fourier transform is interchangeable and the correction of through-plane and in-plane distortions are independent of the y-phase encoding, we can first apply an inverse Fourier transform along the slice-select direction to resolve the excitation profiles, followed by performing in-plane partial k-space reconstruction at each slice location. The accelerated data acquisition can also benefit from recent advances in parallel imaging (26,27) and/or compressed sensing (28).

Another potential means to reduce scan times is to adapt the nominal thickness of each slice such that the largest through-plane distortion in each slice is kept roughly constant. Referring to Eq. [2], through-plane distortion is proportional to the product of field inhomogeneities and slice thickness. This suggests that a thicker slice can be prescribed at a location where field inhomogeneities are small. As long as the largest through-plane distortions in the slice do not exceed the corresponding z-phase encoding FOV, the excitation profile is correctly resolved without compromise in the resolution of z-phase encoding.

CONCLUSION

This article presents a MR imaging technique that effectively eliminates metal-induced distortions with feasible scan times. The key idea is to ensure that all spins in an ROI are excited once and are subject to robust spatial encoding against metal-induced field inhomogeneities. Both the phantom and in vivo results demonstrate the efficacy of the proposed SEMAC technique in obtaining distortion-free MR images near metallic implants. This technique holds great promise for significant clinical impact in evaluation of millions of patients with metallic implants.

REFERENCES

1. Kurtz S, Mowat F, Ong K, Chan N, Lau E, Halpern M. Prevalence of primary and revision total hip and knee arthroplasty in the united states from 1990 through 2002. J Bone Joint Surg Am 2005;87: 1487–1497.
2. Resnick D. Diagnosis of bone and joint disorders. New York: Saunders; 2002.
3. Olsen RV, Munk PL, Lee MJ, Janzen DL, MacKay AL, Xiang QS, Masri B. Metal artifact reduction sequence: Early clinical applications. Radiographics 2000;20:699–712.
4. Eustace S, Goldberg R, Williamson D, Melhem ER, Oladipo O, Yucel EK, Jara H. MR imaging of soft tissues adjacent to orthopaedic hardware: Techniques to minimize susceptibility artefact. Clin Radiol 1997;52:589–594.
5. Ludeke KM, Roschmann P, Tischler R. Susceptibility artefacts in NMR imaging. Magn Reson Imaging 1985;3:329–343.
6. Graf H, Steidle G, Martirosian P, Lauer UA, Schick F. Metal artifacts caused by gradient switching. Magn Reson Med 2005;54: 231–234.
7. Camacho CR, Plewes DB, Henkelman RM. Nonsusceptibility artifacts due to metallic objects in MR imaging. J Magn Reson Imaging 1995;5:75–88.
8. Skare S, Anderson J. Correction of MR image distortions induced by metallic objects using a 3D cubic B-Spline basis set: Application to stereotactic surgical planning. Magn Reson Med 2005;54:169–181.
9. Butts K, Gold GE. Correction of slice profile distortions from metallic devices. In: Proceedings of the 14th Annual Meeting of ISMRM, Seattle, 2006. p 2380.
10. Venook RD, Matter NI, Ramachandran M, Ungersma SE, Gold GE, Giori NJ, Macovski A, Scott GC, Conolly SM. Prepolarized magnetic resonance imaging around metal orthopedic implants. Magnetic Resonance Med 2006;56:177–186.
11. Cho ZH, Kim DJ, Kim YK. Total inhomogeneity correction including chemical shifts and susceptibility by view angle tilting. Med Phys 1988;15:7–11.
12. Butts K, Pauly JM, Gold GE. Reduction of blurring in view angle tilting MRI. Magn Reson Med 2005;53:418–24.
13. Kolind SH, MacKay AL, Munk PL, Xiang QS. Quantitative evaluation of metal artifact reduction techniques. J Magn Reson Imaging 2004;20:487–495.

14. Koch KM, Busse RF, Lewein T, Potter HG, Hinks R, King K. Multiple resonant frequency offset acquisitions for imaging of metallic implants. In: Proceedings of the 16th Annual Meeting of ISMRM, Toronto, 2008. p 1250.
15. Lu W, Butts K, Gold GE, Pauly JM, Hargreaves BA. Towards artifact-free MRI near metallic implants. In: Proceedings of the 16th Annual Meeting of ISMRM, Toronto, 2008. p 838.
16. Koch KM, Hinks R, King K. Empirical and computed B0 perturbations induced by metallic implants. In: Proceedings of the 16th Annual Meeting of ISMRM, Toronto, 2008. p 1180.
17. Nishimura DG. Principles of magnetic resonance imaging. Stanford: Stanford University; 1996.
18. Speier P, Trautwein F. A calibration for radial imaging with large inplane shifts. In: Proceedings of the 13th Annual Meeting of ISMRM, Miami, 2005. p 2295.
19. Guermazi A, Miaux Y, Zaim S, Peterfy C, White D, Genant HK. Metallic artefacts in MR imaging: Effects of main field orientation and strength. Clin Radiol 2003;58:322–328.
20. Graf H, Steidle G, Martirosian P, Lauer UA, Schick F. MRI of hip prostheses using single-point methods: In vitro studies towards the artifact-free imaging of individuals with metal implants. Magn Reson Imaging 2004;22:1097–1103.
21. Glover GH. 3D z-shim method for reduction of susceptibility effects in BOLD fMRI. Magn Reson Med 1999;42:290–299.
22. Constable RT, Spencer DD. Composite image formation in z-shimmed functional MR imaging. Magn Reson Med 1999;42:110–117.
23. Yang QX, Williams GD, Demeure RJ, Mosher TJ, Smith MB. Removal of local field gradient artifacts in T_2^*-weighted images at high fields by gradient-echo slice excitation profile imaging. Mag Reson Med 1998;39:402–409.
24. Busse RF, Hariharan H, Vu A, Brittain JH. Fast spin echo sequences with very long echo trains: Design of variable refocusing flip angle schedules and generation of clinical t_2 contrast. Magn Reson Med 2006;55:1030–1037.
25. Noll DC, Nishimura DG, Macovski A. Homodyne detection in magnetic resonance imaging. IEEE Trans Med Imaging 1991;10:154–163.
26. Pruessmann KP, Weiger M, Scheidegger MB, Boesiger P. SENSE: Sensitivity encoding for fast MRI. Magn Reson Med 1999;42:952–962.
27. Griswold MA, Jakob PM, Heidemann RM, Nittka M, Jellus V, Wang J, Kiefer B, Haase A. Generalized autocalibrating partially parallel acquisitions (GRAPPA). Magn Reson Med 2002;47:1202–1210.
28. Lustig M, Donoho D, Pauly JM. Sparse MRI: The application of compressed sensing for rapid MR imaging. Magn Reson Med 2007;58:1182–1195.